

Weak Hydrogen Bonds as a Structural Motif for Two-Dimensional Assemblies of Oligopyridines on Highly Oriented Pyrolytic Graphite: An STM Investigation

Christoph Meier, Ulrich Ziener,* Katharina Landfester, and Petra Weihrich

Organic Chemistry III/Macromolecular Chemistry and Organic Materials, University of Ulm, Albert-Einstein-Allee 11, D-89081 Ulm, Germany

Received: August 2, 2005; In Final Form: September 9, 2005

We present the STM investigation of four different oligopyridines at the liquid/highly oriented pyrolytic graphite interface. The heteroaromatic compounds are constitutional isomers showing the same overall shape regardless of their actual conformation. On the basis of weak intermolecular C–H···N hydrogen-bonding interactions, different nanopatterns are formed following a simple general concept for the two dimensional self-assembly. The molecules arrange either in linear or in cyclic structures. Though the oligopyridines are achiral, the formation of prochiral trimeric superstructures leads to chiral phases due to the immobilization on the surface. Some of the molecules show polymorphic structures depending on the solvent. The large variety of the presented structures formed by self-assembly of the different oligopyridines which retain the same functional heteroaromatic backbone shall open the possibility of exploiting these patterns as templates for the nanostructuring of surfaces with guests such as small molecules or metal ions for intriguing applications in, for example, catalysis.

Introduction

Surface nanopatterning and two-dimensional (2D) crystal engineering are strongly developing fields of research in the recent years. The bottom-up strategy is a convenient approach for such supramolecular assemblies by using programmed molecular building blocks which self-organize to the desired nanostructures.^{1,2} Hydrogen bonds are highly attractive for this purpose due to their high capability of tailoring the strength of the intermolecular interactions and their directionality, depending on the alignment. In the past few years, the main interest in the investigation of hydrogen-bond assisted self-assembly at the solid/liquid interface with scanning tunneling microscopy (STM) was concentrated on heteroatom X–H···Y hydrogen-bonding directed self-organization with a strong hydrogen donor. The O–H···O hydrogen bond for self-assembly directed ordering was reported for a lot of carboxylic acid derivatives,^{3–13} revealing the suitability of this type of hydrogen bond for surface nanopatterning. Similarly, the N–H···N hydrogen bond was used in 2D assemblies, realized with molecules containing diamine triazine moieties,¹⁴ ureido-*s*-triazine moieties,¹⁵ and with the nucleobase adenine.¹⁶ Both types of hydrogen bonds are mixed in N–H···O hydrogen-bond patterns, realized with interactions between urea groups,^{17,18} amide¹⁹ and imide groups,^{20,21} carbamates,²² chiral formamides,²³ and in O–H···N hydrogen bonds.^{24,25} Besides these well-known comparably strong heteroatom X–H···Y hydrogen bonds, only a few examples of C–H···X hydrogen bonds with weaker hydrogen donors as structure directing units in 2D assemblies are described.^{20,25–32} For example, a prochiral pyridyl-vinyl-benzoic acid (PVBA) on Ag(111) forms dimeric chains which are explained by C–H···O hydrogen bonds besides the O–H···N interactions.²⁵ The same compound forms either homochiral or racemic phases on Cu(100) depending on the substrate cover-

age.³⁰ Both phases seem to be stabilized through lateral tail-to-side C–H···O and tail-to-tail C–H···N hydrogen-bonding interactions. By vapor deposition of terephthalic acid molecules and iron atoms on a Cu(100) surface under ultrahigh vacuum conditions, different metallosupramolecular assemblies are formed which show partially C–H···O hydrogen bonds between ortho-protons of the benzene moieties and the carboxylic groups.^{26,29} The high potential of weak hydrogen-bonding networks in surface structuring was shown with cyanobenzene-substituted porphyrines, providing a C–H hydrogen donor and a sp-hybridized N hydrogen acceptor.²⁷ These chemically functionalized porphyrines form different aggregates on Au(111) stabilized by C–H···NC hydrogen bonds but are limited to linear chains and small tri- or tetrameric aggregates. Recently, we have demonstrated the self-assembly of an oligopyridine at the highly oriented pyrolytic graphite (HOPG)/liquid interface forming highly ordered monolayers which are based on weak C–H···N hydrogen bonds.²⁸

In this paper, we will show that the above-mentioned example²⁸ of weak hydrogen bonds of interacting pyridine moieties (see Figure 1b) can be extended and conceptually used for the design of nanostructured surfaces. A series of oligopyridines is presented which are all constitutional isomers (part a of Figure 1 and Figure 3) and which self-assemble into well-ordered monolayers at the liquid/graphite interface. These self-assemblies are investigated by scanning tunneling microscopy (STM) operated at ambient conditions. The applied molecules differ only in the positions of the N-atoms in the peripheral pyridine rings but exhibit a constant molecular shape. Even conformational (coplanar) isomers do not show a different overall geometry of the molecules. The pyridine–pyrimidine–pyridine backbone of the oligopyridines causes the conformational rigidity due to the preferred transoid NC–CN conformation which is necessary for the control of 2D ordering. Through variation of the positions of the nitrogen atoms in the terminal pyridine moieties, we are able to control the nano-

* To whom correspondence should be addressed. E-mail: ulrich.ziener@chemie.uni-ulm.de.

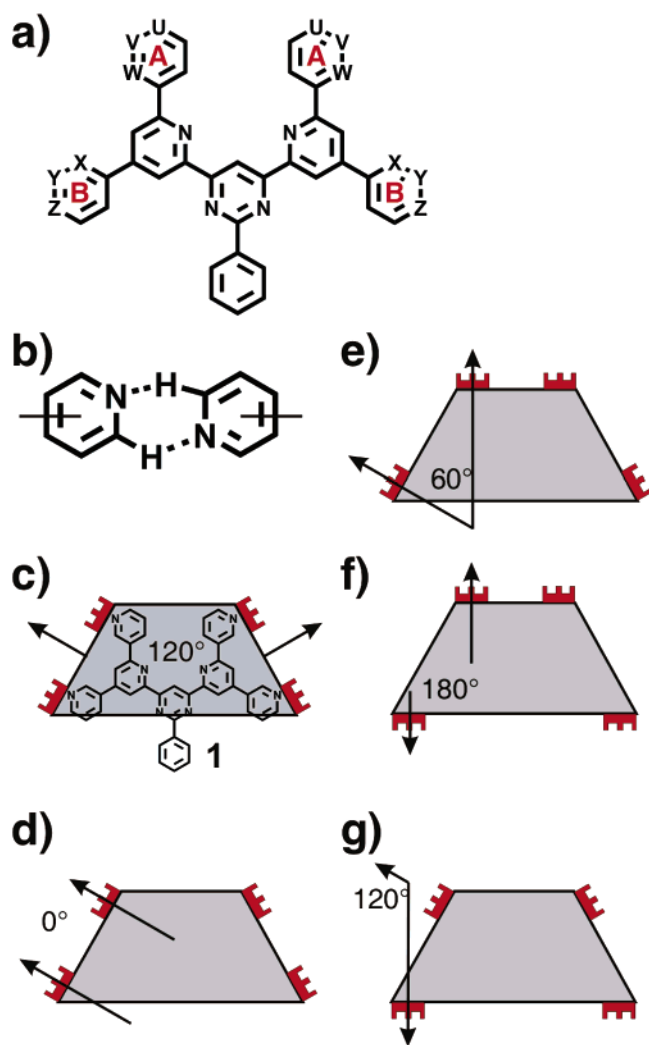


Figure 1. (a) Skeletal structure of the investigated oligopyridines. The letters U–Z indicate all the possible positions of the nitrogen atoms in the terminal pyridine moieties. (b) Double weak hydrogen bonds which might act between the terminal pyridine rings of two neighboring molecules. (c) Overlay of compound **1** (in the less stable conformation, see Figure 3) with a simplified model representing the schematic shape of the molecules and the direction of weak self-complementary double hydrogen-bonding interactions. (d–g) Approximate relative orientation of the hydrogen-bonding interactions which are possible due to the different constitutional isomers.

patterning at the solid/liquid interface via the weak C–H···N hydrogen-bonding interactions.

In Figure 1a, the skeletal structure of the investigated oligopyridines is displayed. The terminal pyridines A and B are designed to provide the hydrogen-bond acceptor functionality via sp^2 -hybridized nitrogen atoms. The possible positions of the nitrogen atoms in the terminal pyridines are represented by the letters U–Z. The principal shape of the molecules can be depicted as a trapezoid with pendant tridents representing the orientation of the self-complementary hydrogen-bonding acceptors (N atoms) and donors (C–H moiety) (Figure 1c). As the orientation of the hydrogen-bonding acceptors is clearly given by the lone pairs of the N-atoms, the donors are less defined because each C–H group can act in principle as the donor. Thus, the orientation of the tridents shows an approximate direction of the whole double hydrogen-bond moiety. Additionally, the flexibility of the terminal pyridine rings has to be taken into account leading to different possibilities of hydrogen-bonding directions and subsequently to different patterns of the

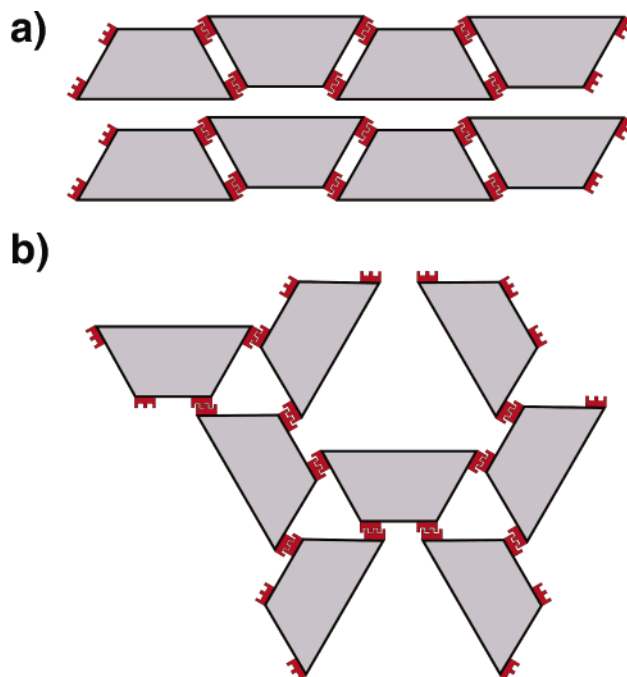


Figure 2. Resulting molecular layer structures of compounds **1–4** are expected to be of (a) zigzag shape (0° relative orientation of the hydrogen-bonding units) or of (b) triangular shape (60° relative orientation of the hydrogen-bonding units).

self-assembled structures. On the other hand, some conformers can be excluded as they are energetically highly unfavorable due to a cisoid NC–CN conformation (especially for W = N in Figure 1a) and as they cannot contribute to intermolecular hydrogen-bonding interactions. Regardless of the absolute direction of the hydrogen-bonding moieties, the relative orientation of the two hydrogen-bonding functions on the left and right side of the molecules, respectively, can adopt certain values (0 , 60 , 120 , and 180° , parts d–g of Figure 1).

Assuming that the molecules in the course of the 2D self-assembly process try to reach fully saturated hydrogen bonds, we expect in principle two different packing patterns in the 2D assemblies, namely, a linear zigzag-like (0° relative orientation of the H-bond interactions) and a threefold trimeric arrangement (60° relative orientation), respectively (Figure 2). For the 120° and 180° relative orientation of the hydrogen-bonding units, no close packing is possible due to steric hindrance. In these cases, we expect that the system escapes from the exigency by either adopting a different conformer or giving up partially the hydrogen bonds.

In the actual compounds, only the combinations of the positions V–Y (**1**), U–Y (**2**), W–Y (**3**), and W–Z (**4**) are occupied by N atoms (Figure 3). Figure 3 indicates the direction of the hydrogen-bonding acceptors which coincide approximately with the orientation of the double hydrogen bonds and tridents in Figures 1 and 2, respectively. The energetically favorable conformations of the molecules in the gas phase are shown in Figure 3 which are not necessarily the preferred conformations in the 2D pattern (see below).

Results and Discussion

Synthesis. Compounds **1** and **2** were synthesized according to the preparation reported in ref 28 by a ring-closure reaction corresponding to the Kröhnke synthesis³³ (Scheme 1). The synthesis of the bispyridinium salt **6** was performed via Stille coupling of 2-phenyl-4,6-dichloropyrimidine with (1-ethoxy)-

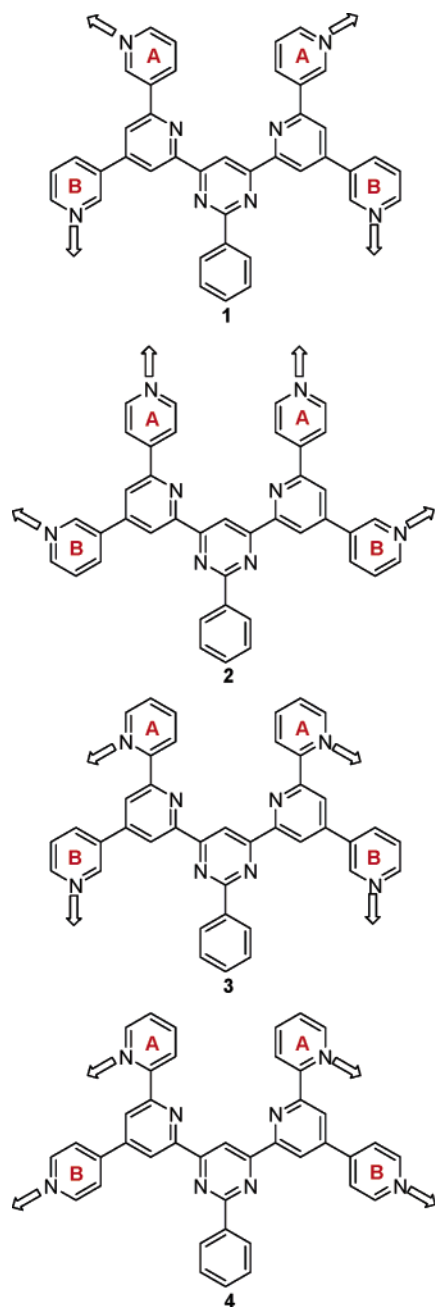


Figure 3. Molecular sketches of the investigated isomeric oligopyridines in the energetically stable conformations in the gas phase. The arrows indicate the preferred direction of the hydrogen-bond acceptors.

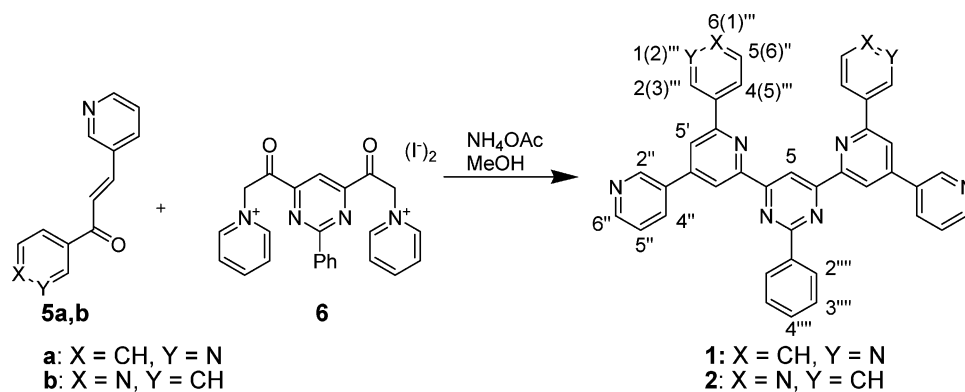
vinyltributylstannane and conversion of the resulting ketone to **6**. The unsaturated ketones **5a** and **b** were derived via a Knoevenagel condensation of 3-pyridine carbaldehyde with 3- and 4-acetyl pyridine, respectively.³⁴ The double Michael addition of **5a**, **b**, and **6** with subsequent cyclization and aromatization resulted in the oligopyridines **1** and **2** in good yields. The phenyl moiety proved to be essential for an efficient synthesis of these compounds. Attempts to synthesize and isolate purely the corresponding derivatives with a hydrogen atom instead of the phenyl group failed due to extremely low solubility. Furthermore, we assume that the phenyl group provides additional stability to the 2D assembly (see below).

STM Investigations of the Oligopyridine Derivatives. It has to be stated that—as the employed compounds are purely (hetero)aromatic without additional alkyl chains—the interpreta-

tion of the STM images proves to be quite difficult due to the absence of functional groups providing for contrast.²⁴ Hence, for an unambiguous interpretation of the STM results, highly resolved images are required which are shown in the following. A precondition for the formation of the proposed hydrogen-bonding interactions is a coplanar adsorption geometry of the oligopyridines and a defined conformation of the terminal pyridine moieties. The coplanar adsorption geometry is privileged by the π - π interactions between the adsorbed molecules and the substrate and can be deduced from the submolecularly resolved STM images shown below. For a noncoplanar conformation of the adsorbed molecules, specific pyridine moieties are slightly lifted off the surface and should appear brighter in the images.³⁵ Instead, we observed a brighter area in the center of the molecules. The ideal conformation determined by a gas-phase Hartree–Fock geometry optimization without fixing dihedral angles is twisted between the terpyridine and phenyl subunits. From the STM images, the conformation of the terminal pyridine moieties cannot be unambiguously deduced. However, the maximization of the hydrogen-bonding interactions in the proposed structures determines clearly the conformation of the pyridine moieties on the surface.

In oligopyridine **1**, the sp^2 orbitals of the nitrogen atoms in the terminal A-pyridine units include an angle of 120° with regard to the C_2 -axis (Figure 3). After the B-pyridine units were flipped, resulting in the slightly less stable conformational isomer ($\Delta E = 2.6$ kJ/mol in the gas phase, see below), both free electron pairs of the N-atoms in rings A and B, respectively, would point in the same direction (see also Figure 1c). Therefore, the interaction forces should lead to chainlike structures (Figure 2a). Indeed, after the addition of a droplet of concentrated solution of **1** in TCB (1,2,4-trichlorobenzene) to the HOPG surface, two polymorphic chainlike structures could be imaged with STM (Figures 4 and 5).

The submolecular resolution of the achiral polymorphic phase (Figure 4a) allows the identification of single molecules in the monolayer. The molecular shape of the investigated oligopyridines is clearly visible and highlighted with a superimposed contour of a single molecule. There are vertical rows observable containing molecules with the same orientation lying front-to-back. The resulting unit cell is of rectangular symmetry, with the lattice constants $a = 2.7 \pm 0.2$ nm and $b = 1.6 \pm 0.2$ nm. From these observations, a model of the monolayer can be easily developed showing periodicities which are in good agreement with the experimental results (Figure 4b). The monolayer structure can be considered as the closed packing possible for the molecular shape of the investigated oligopyridines. Besides the pure-packing criterion, additionally, eight stabilizing hydrogen-bonding interactions per molecule between the terminal A- and B-pyridine rings can be found in the monolayer if we assume the slightly less stable conformational isomer (Figure 4c). From the submolecular resolution of the STM images, a highly accurate model can be deduced which allows even an exact assignment of the participating H-bond donors ($C-H_p$ of the A-rings and $C-H_o$ of the B-rings) as well as an estimation of the hydrogen-bond $H_{o,p} \cdots N$ distances to be 2.5 ± 0.2 Å which is in good agreement with the experimental values of H-bond interactions and also with the theoretical results for pyridine dimers (see below). The estimated value of the $C-H \cdots N$ interaction is not determined from the STM image directly but obtained from the model—which is overlayed to the STM image—by averaging 10 values of the corresponding $H \cdots N$ distances. Thus, the error refers only to the averaging process but not to the accuracy of the model.

SCHEME 1. Syntheses of the Oligopyridines **1** and **2**^a

^a The numbering relates to the assignment of the signals in the ¹H NMR spectra. The numbers in parentheses correspond to **2**.

The monolayer described above is the dominating surface pattern of **1** on HOPG. Additionally, a polymorphic phase covering about 10% of the surface area could be observed (Figure 5a). The submolecularly resolved STM image allows again a direct assignment of the molecules and their arrangement in the monolayer.

The monolayer structure can be deduced from the more close-packed structure (see above, Figure 4) by decreasing the angle in the rectangular unit cell from 90° to 78°. Hence, the unit cell symmetry is changing from rectangular to rhombohedral. The molecules, previously lying front-to-back in a row, are now slightly shifted toward each other about 0.7 nm. This leads to a non-close-packed chiral monolayer. The unit cell parameters are $a = 2.9 \pm 0.2$ nm and $b = 1.6 \pm 0.2$ nm, and the angle between a and b is found to be $78 \pm 1^\circ$. We do not expect an excess of one of the chiral phases, but the corresponding enantiomorphic phase could not be imaged yet probably due to the overall low surface coverage of the two chiral phases. Thus, the “missing” of the second phase is caused by a problem of statistics. The black ellipsoidal depressions visible in the STM image can be assigned to cavities in the monolayer. There are two types of cavities present in the monolayer, indicated with arrows in parts a and b of Figure 5. They are distinguishable through the functional groups enclosing the cavities. One type is enclosed by two phenyl rings (red arrows); the other type is enclosed by a phenyl ring and a terminal pyridine ring (white arrows). Compared to the polymorphic phase discussed above, these cavities are a direct consequence of the displacement of the molecules. The hydrogen-bonding pattern is displayed in Figure 5c. As above, the molecules are coplanarly adsorbed. The assumed conformational isomer can establish eight weak C–H···N hydrogen bonds per molecule as well. Unlike the achiral polymorphic structure (Figure 4), two different bonding sites per molecule are used, leading to the observed non-closed-packed structure. Here, the hydrogen-bond donors are at one molecular side C–H_o (A-ring) and C–H_p (B-ring) and at the other side C–H_p (A-ring) and C–H_o (B-ring), respectively. Though we could not predict unambiguously which H-bond donor will participate preferably in the 2D assembly of oligopyridine **1**, the principle of the linear arrangement due to the angle of 0° of the hydrogen-bonding units is maintained (see Figure 2a). We also performed STM experiments with different solvents to reveal if the formation of the two polymorphs of **1** can be influenced eventually by the solvent. So far, the formation of a monolayer was not observed either from 1,3-dichlorobenzene or from 1-phenyloctane, which could be visualized by STM.

A further proof of the concept of weak hydrogen bonds C–H···N as a structural motif for the design of 2D assemblies could be given by the specific formation of the triangular structure (Figure 2b) through tailor-made molecules with the angle of 60° between the directions of the hydrogen-bonding units at the right and left side of the molecules, respectively (Figure 1e and Figure 2b). This structural condition is realized in oligopyridine **2**, where the position of the N-atoms in the A-pyridine moieties has changed from meta to para compared to **1**. STM investigations of **2** from a concentrated solution in TCB at the solid/liquid interface revealed the spontaneous formation of a physisorbed well-ordered monolayer with threefold symmetry. Unfortunately, the images could only be obtained in poor resolution and are therefore not displayed. The resolution could be enhanced by adding a drop of pure 1,3-DCB (1,3-dichlorobenzene) to the already covered HOPG surface (Figure 6). The STM investigation directly from a saturated solution of **2** in 1,3-DCB reveals other tunnel contrast characteristics than those from the above-mentioned procedure. Due to its poor resolution, it is not further discussed. The formation of monolayers occurred from PO (1-phenyloctane), also, showing the same characteristics of a threefold symmetry of the structure. Figure 6 shows a typical high-resolution large scan area STM image. A periodic superstructure, formed by depressions in the STM image, is highlighted with white threefold ordered circles. Considering this superstructure, it is possible to determine two chiral phases, separated by a domain border, indicated in the STM image with a white line.

Both chiral phases were imaged with submolecular resolution. The magnification of the homochiral R-phase is shown exemplarily which allows a more detailed view into the molecular structure of the monolayer (Figure 7a). The image is submolecularly resolved. The absence of functional groups which provide chemical contrast, for example, nonaromatic moieties as alkyl chains with σ -orbitals, makes it difficult to distinguish between single molecules. Nevertheless, the bright disks with a depression in the center can be allocated to the benzene rings and the terminal pyridine rings, respectively, due to theoretical studies³⁶ which leads us to a model shown below. In this molecular monolayer, the unit cell exhibits rhombic symmetry with the lattice constants $a = 2.8 \pm 0.2$ nm and $b = 2.9 \pm 0.2$ nm. The lattice vectors enclose an angle of $125 \pm 1^\circ$.

The molecular structure of the monolayer of **2** is, compared to **1**, more complex. The building block is composed of three C_{2v} -symmetric molecules of **2** rotated 120° against each other and self-assembled into a threefold prochiral aggregate (Figure 7b). The intermolecular hydrogen-bonding pattern which is

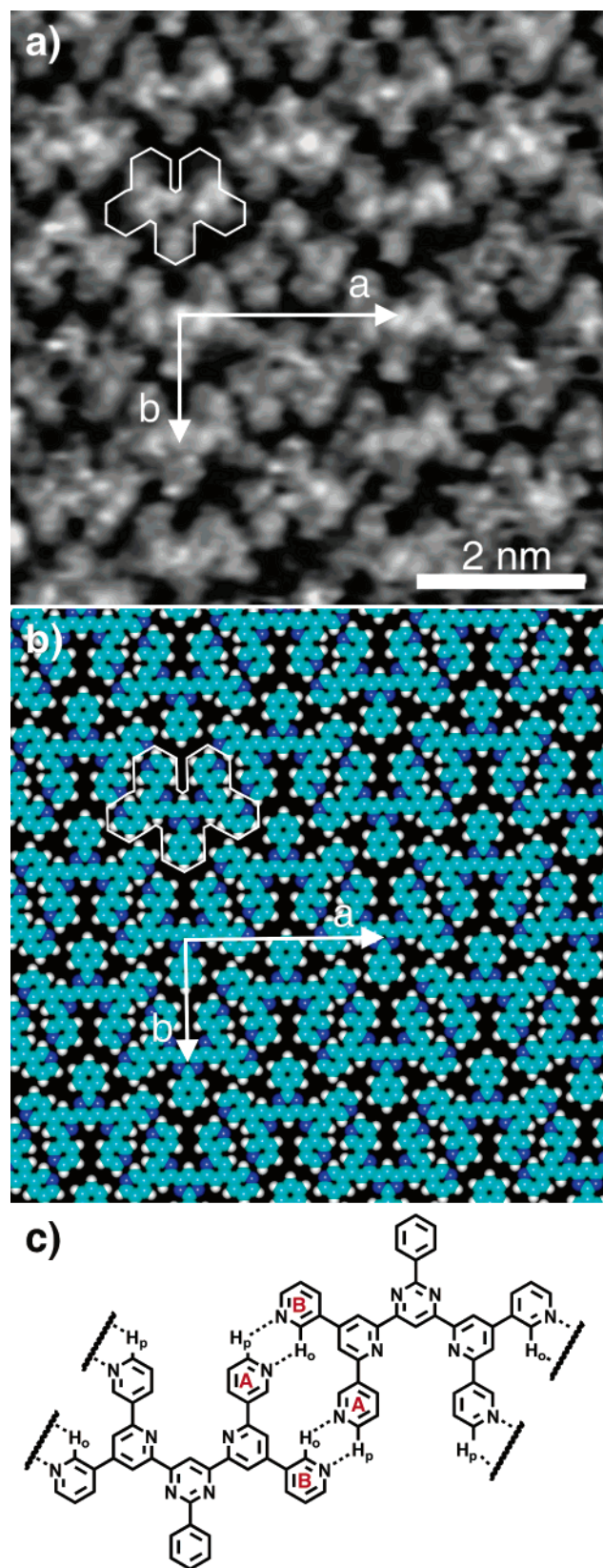


Figure 4. (a) High-resolution STM image of **1** from TCB physisorbed on HOPG, $I_{\text{set}} = 15.4$ pA, $V_{\text{set}} = -882$ mV. (b) Proposed packing model of the monolayer with $a = 2.7$ nm and $b = 1.6$ nm. (c) Molecular sketch of a part of the monolayer model of **1** on HOPG to reveal the hydrogen-bonding interactions.

specific for the position of the nitrogen atoms in the terminal pyridine moieties is displayed in Figure 7c. Contrary to compound **1**, the coplanar adsorbed molecules of **2** at the

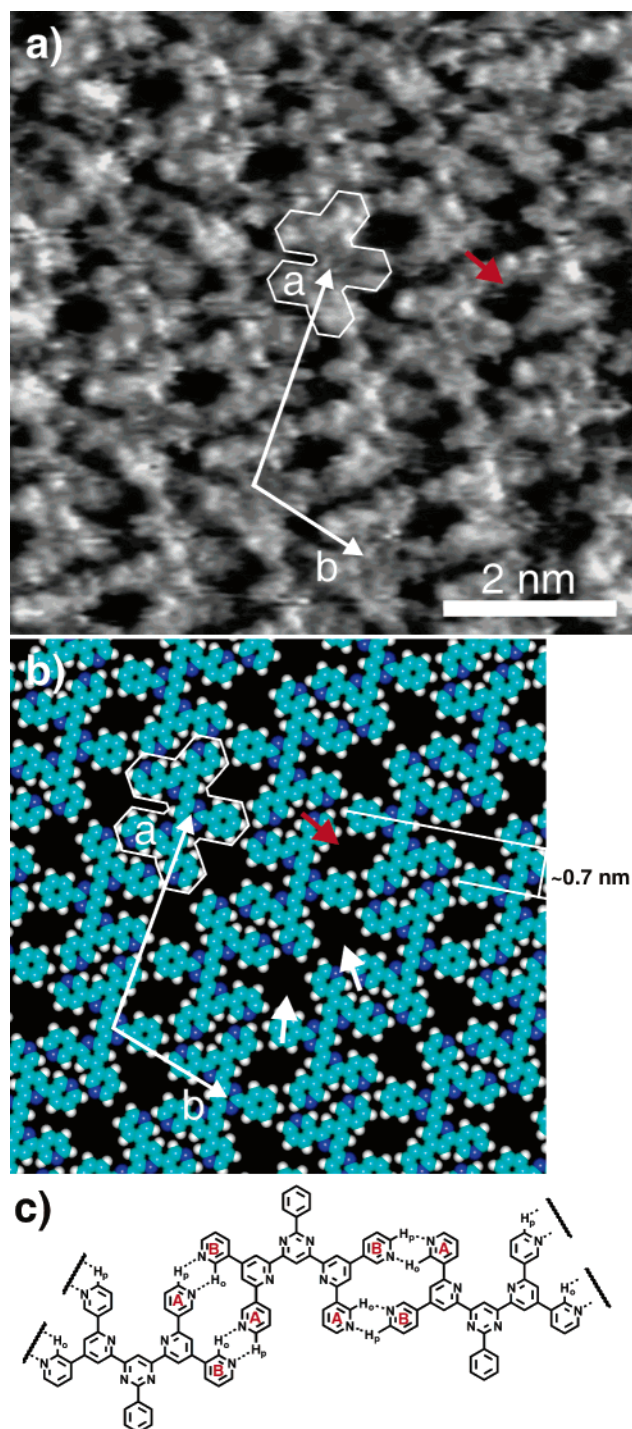


Figure 5. (a) High-resolution STM image of the observed polymorphic phase of **1** from TCB on HOPG covering the minor surface area, $I_{\text{set}} = 19.4$ pA, $V_{\text{set}} = -961$ mV. The shape of a single molecule is superimposed. (b) Model of a magnified area in part a. For clarity, the shape of a single molecule with the same position and orientation as in part a is superimposed. The arrows of different colors indicate the two types of cavities, $a = 2.9$ nm and $b = 1.6$ nm. (c) Molecular sketch of a part of the monolayer model for the polymorphic structure of **1** physisorbed on HOPG to reveal the hydrogen-bonding interactions.

interface exhibit the energetically favorable conformation regarding the terminal pyridine moieties (cf. Figure 3) as they are able to form eight stabilizing intermolecular hydrogen-bonding interactions per molecule (Figure 7c). The hydrogen-bonding donors are unambiguously the C–H_m (A-ring) and C–H_p (B-ring) units. On the surface, symmetry breaking of the prochiral trimers occurs, leading to a racemic segregation. Thus,

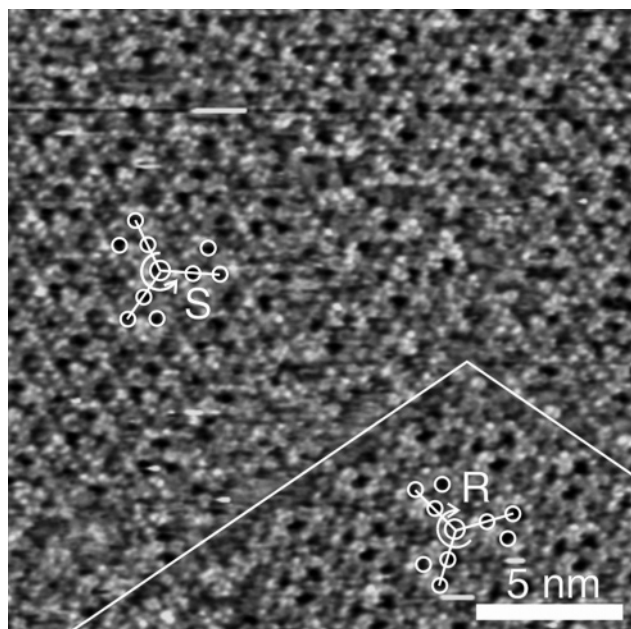


Figure 6. Large scan area STM image of **2** on HOPG from TCB after adding 1,3-DCB, $I_{\text{set}} = 8.9$ pA, $V_{\text{set}} = -849$ mV. White circles are superimposed to the triangular arranged black depressions to reveal ordering and chirality. The domain border between the two homochiral phases is indicated.

the enantiomeric trimers separate and appear in different domains. To our knowledge, this is the first report of racemic segregation of achiral molecules on an achiral surface, determined by a prochiral supramolecular single-component aggregate. For the achiral molecules themselves, no 2D chirality is induced through the adsorption on the surface because of their C_{2v} symmetry. Until now, symmetry breaking of prochiral molecules on a substrate or substrate-induced chirality^{29,37} or the formation of prochiral supramolecular aggregates³⁰ and complexes¹³ composed of prochiral monomers are described. For example, the prochiral C_s -symmetric molecule purine undergoes racemic segregation on naturally grown MoS_2 , whereas on synthetic HOPG, the monolayers consist of a racemic mixture of Si- and Re-adsorbed purine molecules.³⁸ The prochiral C_s -symmetric 1,2,4-benzenetricarboxylic acid (tmla) forms prochiral $\text{Fe}(\text{tmla})_4$ complexes with codeposited Fe atoms.¹³ Another prochiral molecule, a C_s -symmetric pyridyl-vinyl-benzoic acid (PVBA), forms a racemic butterfly phase above a critical coverage on $\text{Cu}(100)$, consisting of a 1:1 mixture of 2D chiral tetrameric building blocks.³⁰ Both 2D chiral supramolecular aggregates, $\text{Fe}(\text{tmla})_4$ and $(\text{PVBA})_4$, consist of *prochiral* monomers, whereas the 2D chiral supramolecular aggregates presented here are formed from *achiral* monomers.

Compounds **1** and **2** self-assemble specifically into trimeric and linear structures on the graphite surface, respectively, due to the relative orientation of the hydrogen-bonding units on each side of the molecules (see above). In the oligopyridine **3**, the angle between the direction of the hydrogen-bonding acceptors (N-atoms of the terminal pyridine rings A and B) is in the energetically favorable conformation 60° and in the corresponding less stable conformer -60° (Figure 3). From these findings, one should expect a trimeric structure similar to that found for **2**. A closer look reveals that the ortho-linkage of the A-pyridine ring might cause problems for the H-bonds because of steric hindrance. Additionally, the formation of the less stable conformational isomer could also favor the linear arrangement of the molecules due to the orientation of the H-bond acceptors in the B-pyridine rings perpendicular to the edge of the trapezoid

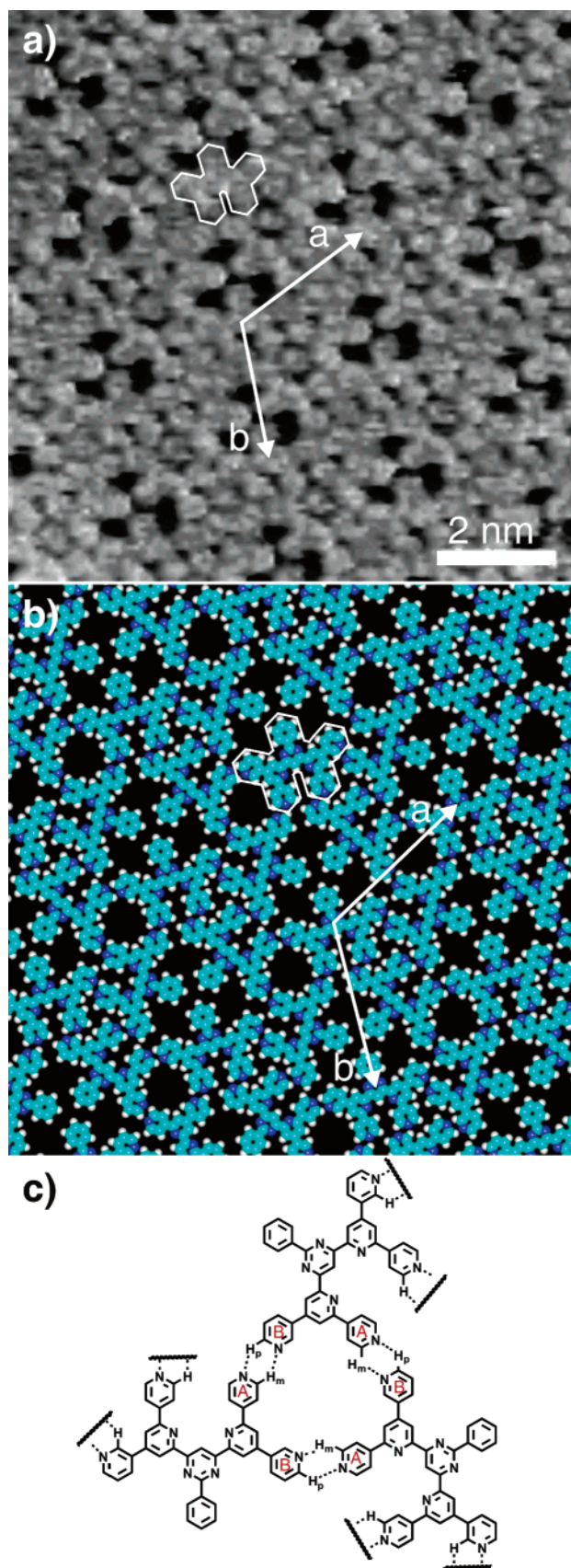


Figure 7. (a) Submolecularly resolved STM image of the homochiral R-phase area of **2** from TCB showing the (hetero)aromatic moieties, $I_{\text{set}} = 13.4$ pA, $V_{\text{set}} = -862$ mV. (b) Model of the monolayer with superimposed molecular shape and a unit cell with $a = 3$ nm, $b = 3$ nm, and $\angle_{a,b} = 120^\circ$. The high consistence between the model and the STM image is clearly visible. (c) Molecular sketch of the prochiral supramolecular trimer of **2** physisorbed on HOPG.

as it is present in the packing pattern of compound **1** (Figure 4). Hence, from the ambiguous structural situation in compound **3**, both structural patterns (linear zigzag and cyclic assembly, respectively) are anticipated at the liquid/solid interface.

When we performed the deposition of **3** in TCB on HOPG, we could not observe any monolayer formation. Self-assembly from 1,3-DCB and PO solution, respectively, led to patterns which could be successfully investigated by STM. Figure 8a shows a typical STM image of a physisorbed monolayer of oligopyridine **3**, deposited onto HOPG from 1,3-DCB.

The STM picture is distorted in the slow scan direction and is therefore not submolecularly resolved. Nevertheless, on the basis of the previous results with the strongly related compounds **1** and **2**, a clear and convincing model for the 2D assembly of **3** can be developed. The threefold arranged black dots indicate the presence of a threefold molecular superstructure as the investigated oligopyridines do not exhibit a threefold symmetry. Additionally, we assign the bright spots in the STM image to the area around the pyrimidine rings in the centers of the molecules (see below). With regard to H-bonding interactions, consequently, only one convincing model can be developed which corresponds to both the measured unit cell and the threefold voidal superstructure. The molecular structure formed by **3** at the liquid/solid interface between HOPG and 1,3-DCB is similar to the structure observed for **2**. The unit cell shows rhombic symmetry, containing two molecules. The lattice constants were determined to be $a = 2.9 \pm 0.2$ nm, $b = 2.6 \pm 0.2$ nm, and $\angle_{a,b} = 118 \pm 1^\circ$, which is in good accordance with the proposed model (Figure 8b). As in **2**, the monolayer structure can be built up from a prochiral threefold molecular superstructure formed by three achiral molecules, rotated 120° against each other. Contrary to **2**, no chiral discrimination on the surface occurs as the monolayer consists of a racemic mixture of both enantiomeric trimers. A molecular sketch in Figure 8c presents the hydrogen-bonding pattern in a trimer. The specific position of the nitrogen atoms in the terminal pyridine moieties in the meta and para positions leads to a less densely packed structure than that observed for **1** and **2**. The *N,N*-transoid conformation of the A-pyridine moiety is evident, though not the conformation of the terminal B-pyridine moiety. The adsorbed less stable conformational isomer ($\Delta E = 10.5$ kJ/mol) can form four nearly linear intermolecular C—H \cdots N hydrogen-bonding interactions, which stabilize the structure on the surface. In the case of **3**, a different geometry of the binding subunits compared to the calculated double bound dimer (see below) and to the structures observed for the other oligopyridines **1** and **2** occurs. We suggest that the hydrogen-bonding donors are assigned to the C—H_p groups of the A-rings and the acceptors are represented by the N-atoms of the B-rings. The N-atoms of the A-rings do not participate in intermolecular hydrogen bonding but rather contribute to further intramolecular H-bond stabilization due to the transoid NC—CN conformation.

Surprisingly, we observed a different surface structure when using PO as the solvent. Figure 9 shows a typical large scan area STM image of a physisorbed monolayer of oligopyridine **3** deposited on HOPG from PO.

Eye-catching is the lamellar structure with alternating bright and dark lamellae. The dark lamellae show all the same width of 1.4 ± 0.2 nm, though the bright lamellae exhibit a statistical alternating lamella width of 3.9 ± 0.2 and 5.0 ± 0.3 nm. A detailed view of the STM image showing one lamella allows a deeper insight to the molecular assembly (Figure 10a). The molecular arrangement in the bright area can be partially derived from the STM image but not in the dark area due to the loss of

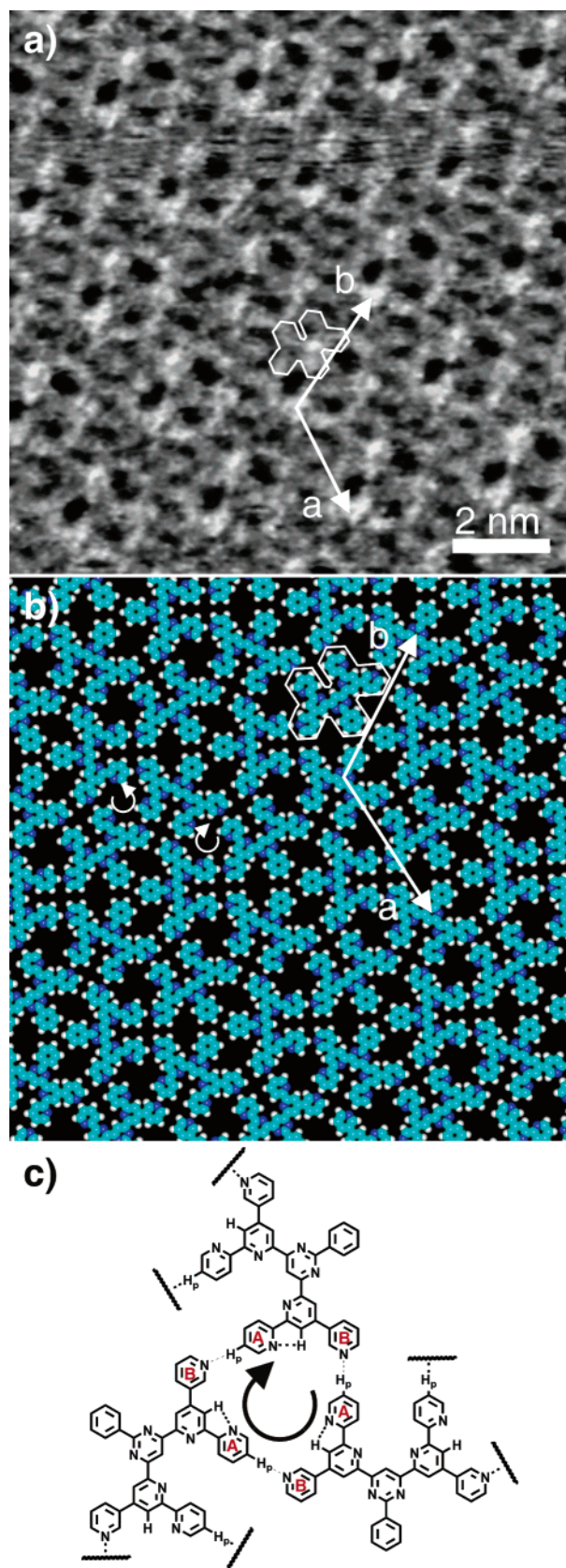


Figure 8. (a) STM image of **3** physisorbed on HOPG from 1,3-DCB. Bright spots can be allocated to the center of the molecules, $I_{\text{set}} = 19$ pA, $V_{\text{set}} = -470$ mV. (b) Tentative molecular model of the monolayer formed by **3** with a superimposed unit cell, $a = 3$ nm, $b = 3$ nm, and $\angle_{a,b} = 120^\circ$. The circular arrows clarify the racemic composition of the monolayer. (c) Molecular sketch of the supramolecular prochiral trimer of **3** physisorbed on HOPG from 1,3-DCB revealing the hydrogen-bonding interactions and the prochirality.

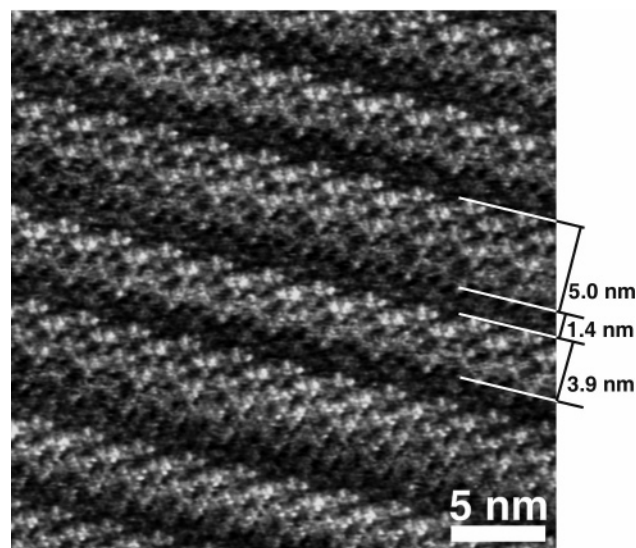


Figure 9. Large scan area STM image of **3** physisorbed on HOPG from PO, $I_{\text{set}} = 9.9$ pA, $V_{\text{set}} = -306$ mV. The lamellar structure consists of alternating bright and dark stripes with widths of 1.4 ± 0.2 (dark), 3.9 ± 0.2 (bright), and 5.0 ± 0.3 nm (bright), respectively.

contrast. We made several attempts to obtain images of **3** with an increased resolution by scanning in different areas of the monolayer and applying new tips, but the presented images are the ones with the highest resolution. Other tips made from tungsten which were electrochemically etched showed even worse results presumably due to the fast oxidation of the tip under ambient conditions. One could assume that the dark/bright contrast arises from two different molecular species such as, for example, alternating rows of **3** and solvent, but there is no reason for the statistical formation of rows of **3** of different width (corresponding to the bright stripes). Additionally, the ratio of the width of the stripes is an integer (“dark/bright/bright” = 1:3:4). Hence, we assume that the alternating bright/dark contrast of the lamellae is caused by solvent effects (see below) and that the molecular structure in the dark area of the STM image is a consequential prosecution of the obvious molecular structure in the bright area. In this case, a satisfying interpretation encounters the same problem as with the STM images of the same compound obtained from 1,3-DCB. The principle difference in the monolayer structures obtained from the two different solvents is obvious. The clearly visible lamellar superstructure can be explained with a linear arrangement of the molecules. Taking a closer look at the STM image, one can discover features similar in shape to the frontier orbitals of compound **3** (see below). The lamellar superstructure, the imaged features of the electronic structure, and the consideration of a convincing hydrogen-bonding pattern allow us to propose a tentative model for **3** physisorbed on HOPG from PO. In this solvent, we propose a chainlike 2D assembly of the molecules on the basal plane of graphite, which corresponds to the second expected 2D assembly arising from the molecular constitution of **3** (see above). This arrangement of the molecules is similar to the chiral polymorph of **1** on HOPG (see Figure 5) but quite different from **2** (see Figures 6 and 7).

The unit cell shows rhombohedral symmetry. The parameters were determined as $a = 1.7 \pm 0.2$ nm, $b = 3.1 \pm 0.2$ nm, and $\angle_{a,b} = 105 \pm 2^\circ$, which substantiates the proposed tentative model. Additionally, the lamellae are shifted about 0.5 nm along their main axis. If we assume that the less stable coplanar configurational isomer is adsorbed ($\Delta E = 10.5$ kJ/mol), then four intermolecular hydrogen bonds per molecule can be formed

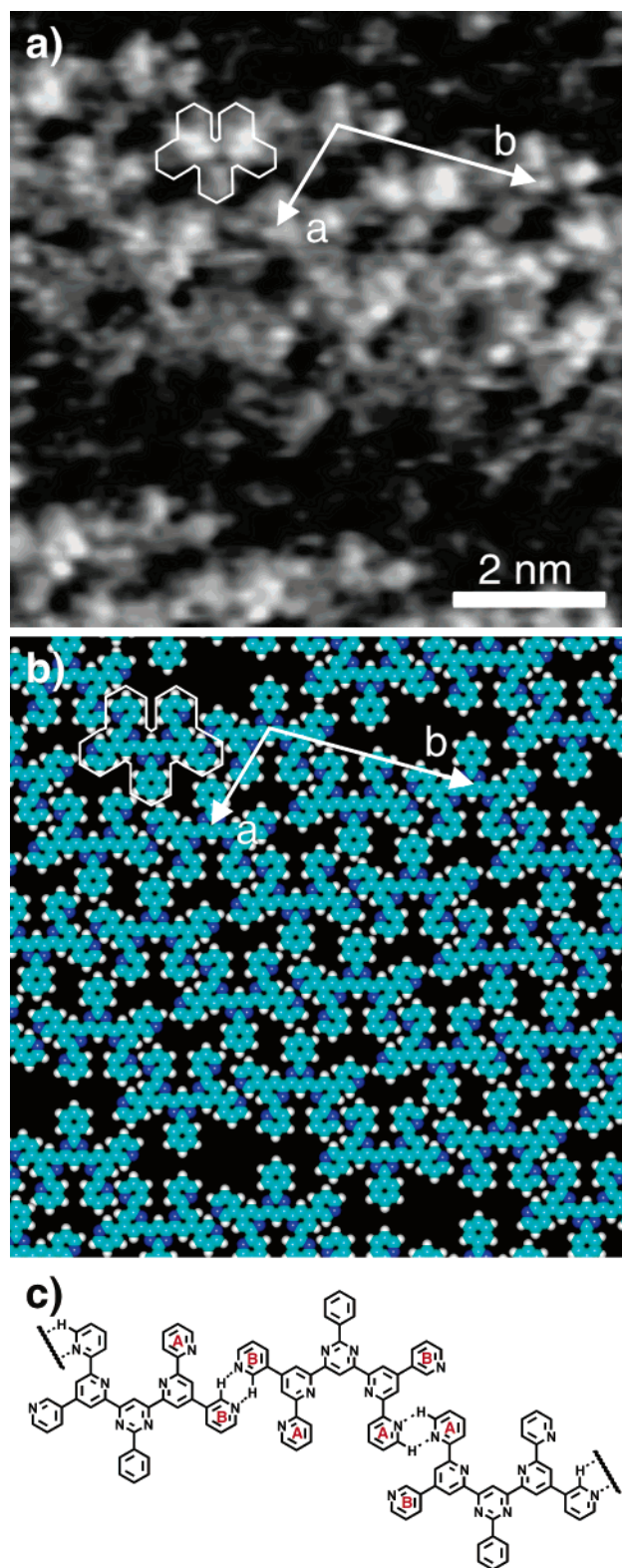


Figure 10. (a) Magnification of a single lamella in Figure 9. (b) Tentative molecular model for **3** at the solid/liquid interface between HOPG and PO, $a = 1.8$ nm, $b = 3.1$ nm, and $\angle_{a,b} = 107^\circ$. (c) Molecular sketch revealing the hydrogen-bonding interactions stabilizing the monolayer of **3** on HOPG, deposited from PO.

to stabilize the structure (Figure 10c). Only interactions between two A- and two B-pyridine moieties, respectively, take place, all other so far presented assemblies rely on a complementary hydrogen-bonding pattern (A–B interaction). The intermolecular bonding interactions show again the same geometry as the

calculated structure for the dimer with double hydrogen bonds (see below).

Despite the large number of publications dealing with self-assembly at the liquid/solid interface, only a few consider the solvent dependency of the observed 2D patterns. The influence of solvents to the adsorption and mobility of adsorbed molecules on graphite was reported.³⁹ Solvents may also affect the 2D pattern through tuning the intermolecular hydrogen-bond configuration⁴⁰ or through competitive adsorption of solvent molecules on the substrate, as assumed for PO.⁴¹ Recent publications deal with the influence of the solvent through coadsorption of solvent molecules into the 2D structure of the solute.^{6,42} In 1,3-DCB, which is a polar solvent with hydrogen-bonding capabilities, the solvation heat of the polar oligopyridine **3** is higher than that in PO. Therefore, the expected free energy is lower in the polar solvent than that in the unpolar solvent. Assuming that these differences in energy of the two solutions are also present at the adlayer/liquid interface leads to the conclusion that the assembly in 1,3-DCB (Figure 8) is more favorable than the one in PO (Figure 9). Furthermore, the enhanced solubility in the polar solvent leads to a destabilization of the solute–surface interaction. The influence of the better solubility might be an explanation why it was impossible to obtain images of **3** on HOPG from TCB, the one with the best solubility among the used solvents. Both effects, differences in free energy and solubility, should reduce the barrier height for the adsorption and desorption of **3** in 1,3-DCB. The mobility is thereby increased and allows the molecules to optimize both their adsorption sites and their hydrogen-bonding interactions. Note that the stabilization energy in 1,3-DCB is one-third higher than that in PO, though the packing density of the former is lower. Contrary to **3**, oligopyridine **1**, which differs only in the position of the N atoms in the A-rings from **3**, could only be imaged successfully from TCB. Experimentally, we observed a very low solubility for **1** in 1,3-DCB and PO, too low to allow the molecules to form highly ordered monolayers. Besides these solubility effects, recent studies indicate that solutions at the onset of crystallization can form structure clusters that control the structure of the precipitate.^{43–45} In our case, we suggest the existence of different molecular aggregates in solution depending on the nature of the solvent. To get more insight to the role of the different electronic and steric features of the solvent on the formation of the 2D layers in our further research, the solvent will be systematically varied from TCB to 1,3-DCB, 1,2-DCB, and chlorobenzene, respectively. Additionally, we also will apply a series of aromatic solvents with reduced H-bonding capability like mesitylene, *o*-, *m*-, and *p*-xylene, and toluene. Furthermore, we have started to investigate the principal influence of the solvent on self-assembly by studying the 2D nanostructures under UHV (ultrahigh vacuum) conditions without any solvent present.

Recently, we reported on a highly ordered self-assembled monolayer of compound **4**.²⁸ From the relative orientation of the hydrogen-bonding units on each side of the molecule (0°, see Figure 1d and Figure 3), a linear arrangement in the 2D structure (Figure 2a) similar to the 2D structure of **1** is expected. After the application of a drop of concentrated solution of **4** in PO to the graphite surface, a spontaneously formed monolayer as shown in Figure 11 was observed. The STM image is not submolecularly resolved (see above), but the periodicities and the imaged monolayer features are quite different to the STM image of the same compound, deposited from TCB (Figure 12). Deposited from PO, the molecules self-assemble into a monolayer with a unit cell of rhombohedral symmetry. This unit cell

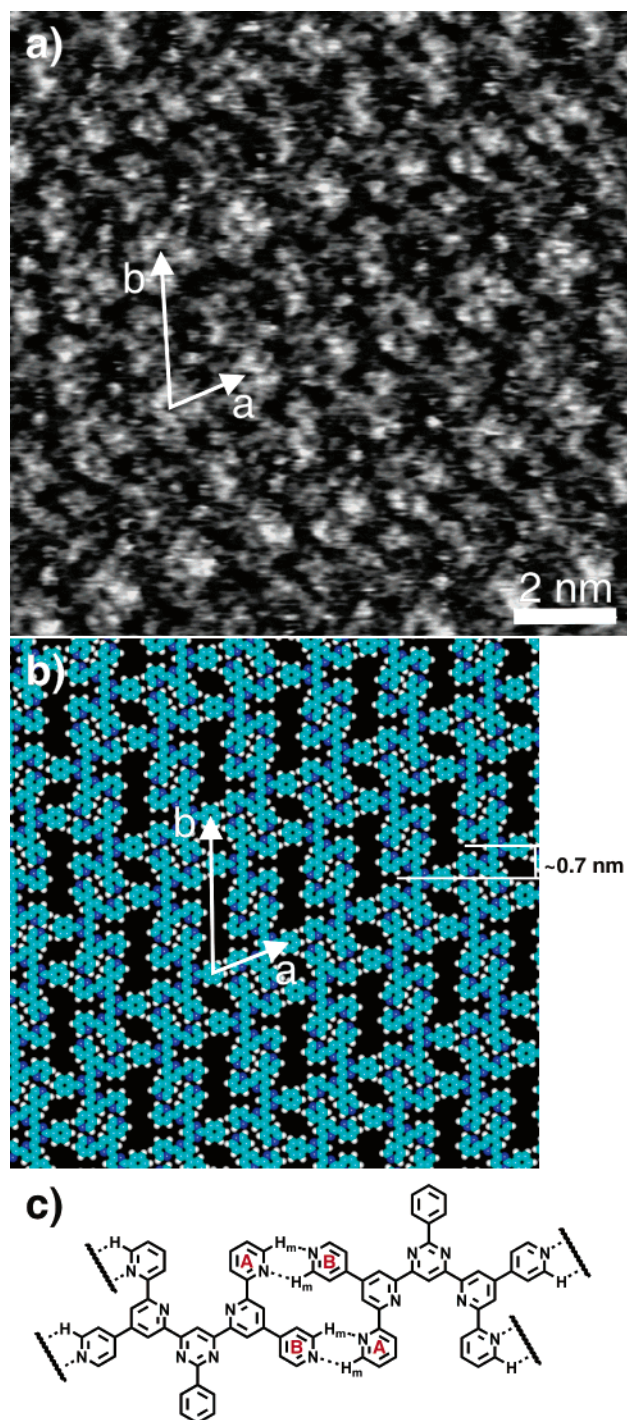


Figure 11. (a) STM image of **4** in PO with $a = 1.7 \pm 0.2$ nm, $b = 3.2 \pm 0.2$ nm, and $\angle_{a,b} = 72 \pm 1^\circ$; $I_{\text{set}} = 12$ pA, $V_{\text{set}} = -758$ mV. (b) Tentative model for **4** physisorbed on HOPG from PO, $a = 1.7$ nm, $b = 3.2$ nm, and $\angle_{a,b} = 70^\circ$. (c) Molecular sketch revealing the hydrogen-bonding interactions between two adjacent molecules in the monolayer.

geometry and the hydrogen-bonding abilities of compound **4** reduce the number of possible molecular structures to a few. In the most convincing model (Figure 11b), the rhombohedral unit cell contains two molecules. The unit cell parameters obtained from the tentative model in Figure 11b are in good accordance to the parameters obtained from the STM image. In the proposed model, the molecules self-assemble into linear chains with two adjacent molecules rotated 120° toward each other. The molecules of adjacent chains are not lying front-to-back. As in the chiral polymorph of **1** (Figure 5), the molecules are shifted about 0.7 nm in direction of the chains. Figure 11c reveals the

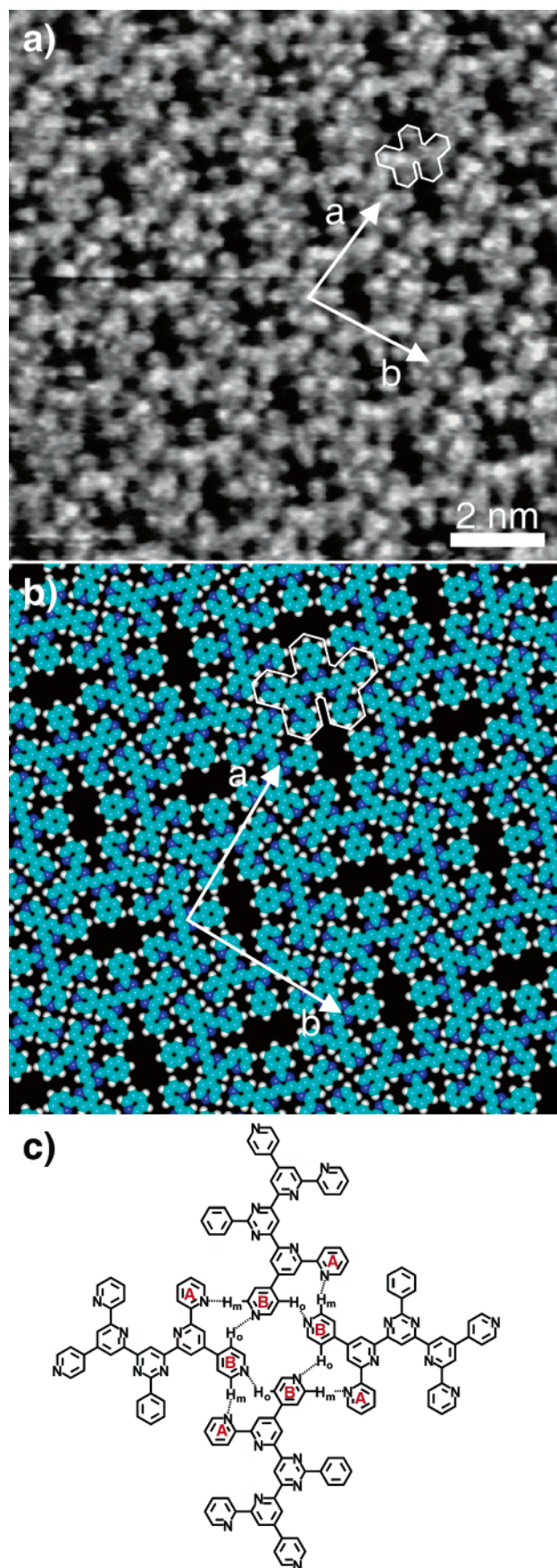


Figure 12. (a) Reexamined STM image of oligopyridine **4** adsorbed on HOPG from TCB, $I_{\text{set}} = 84$ pA, $V_{\text{set}} = -1$ V. (b) Magnified molecular model area for **4** physisorbed on HOPG, $a = 3$ nm, $b = 3$ nm, and $\angle_{a,b} = 90^\circ$. (c) Molecular sketch of the molecular structure of **4** physisorbed on HOPG revealing the hydrogen-bonding interactions.

suggested hydrogen-bonding pattern in a chain. Four double bound pyridine subunits stabilize the structure, resulting in eight hydrogen-bonding interactions per molecule with the C–H_m groups as donor units.

When the monolayer STM image in Figure 11a is compared with a reexamined STM image of **1** on HOPG from TCB (Figure 12), the difference is unambiguous. The submolecular resolution allows the identification of single molecules, supporting the earlier proposed model.²⁸ As already mentioned, the absence of functional groups with an electronic structure different to the aromatic oligopyridine (e.g., alkyl chains with their σ -orbitals) makes it difficult to distinguish between single molecules. A closer look at the STM image allows the identification of single molecules and the molecular arrangement. The square symmetry of the unit cell is obvious, contrary to the rhombohedral unit cell of the monolayer observed in PO (Figure 11). The monolayer structure with square symmetry can be hardly expected from the concept of 2D assembly of these oligopyridines described in the Introduction, but it can be still understood on the basis of the weak hydrogen bonds in the special case of compound **4**.

The model of the molecular arrangement (Figure 12b) favors the molecules in their lowest energy conformation and shows the same periodicities as the STM image (Figure 12a). The monolayer of **4** contains ellipsoidal directionally alternating voids with distances $a = b = 3.1 \pm 0.2$ nm. The unit cell is of square symmetry, containing four molecules. In Figure 12c, the sketch of a tetramer of **4** as observed on HOPG is displayed, revealing the hydrogen-bonding pattern occurring through the specific position of the nitrogen atoms in the terminal pyridine rings. A coplanar conformation on the surface is assumed for the same reason as already mentioned. Unlike above, the configuration of the oligopyridines on the graphite surface is unambiguous. The energy difference to the next less stable configurational isomer, having the A-pyridine in *N,N*-cisoid conformation to its neighboring pyridine, was calculated to be 70 kJ/mol higher, due to repulsive forces of the lone pairs of the nitrogen atoms and the loss of four weak intramolecular hydrogen bonds. Furthermore, the assumed molecular structure in the vicinity of the HOPG surface is in accordance with the observed structures of related compounds in solution and in the solid state.^{46–49} Therefore, eight intermolecular, weak hydrogen-bonding interactions per molecule can be formed, stabilizing the monolayer. The C–H_m and C–H_o groups of the B-pyridine moieties exhibit the hydrogen-bond donors, and the N-atoms of both types of rings represent the acceptors thus showing three hydrogen-bonding interactions per B-ring and only one per A-ring (Figure 12c). The stability of this exceptional 2D structure is based on the high stabilization energy of each intermolecular hydrogen bond (see below).

Theoretical Calculations Oligopyridines **1–4** offer functional groups with hydrogen donor and acceptor capabilities. To receive an impression about the interaction forces, we calculated the stabilizing energy and the optimal geometry of the pyridine dimers in the gas phase at the MP2/6-31G(d,p) level of theory as a model for the interactions of the more complex oligopyridines **1–4**. Figure 13 gives an illustration of the observed interactions of the pyridine dimers.

The N...H interatomic distance of the double bound dimer was calculated to be 2.53 Å, and the N...H interatomic distance of the single bound dimer was calculated to be 2.51 Å. Both distances are shorter than the van der Waals distance of 2.74 nm. The interaction energy was calculated to be 13.4 kJ/mol for the double bound dimer and to be 9.7 kJ/mol for the single

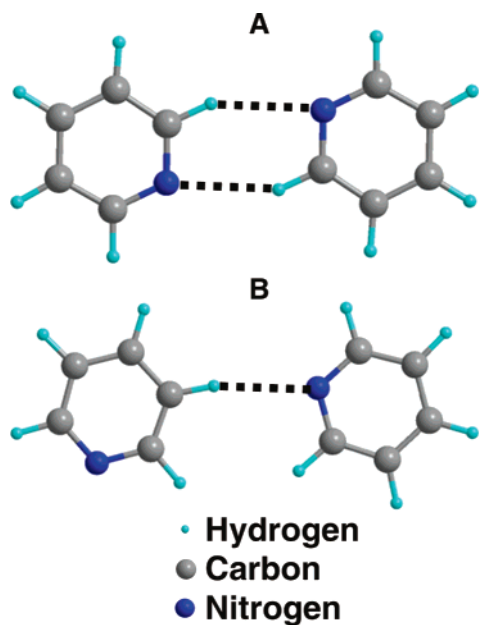


Figure 13. Calculated molecular aggregations of two coplanar pyridine dimers: A, double bound dimer; B, single bound dimer.

bound dimer. The longer $\text{N}\cdots\text{H}$ distance and the lower stabilization energy per H-bond of the double bound dimer can be explained with a less favorable $\text{C}-\text{H}\cdots\text{N}$ bonding angle. These energies are comparable to the experimentally determined energy of heteroatom $\text{X}-\text{H}\cdots\text{Y}$ hydrogen-bonding interactions and, for the double bound dimer, to theoretical results obtained from former DFT calculations.⁵⁰

To fortify our molecular assignment, we calculated the shape of the frontier molecular orbitals of the compounds **1–4** in their coplanar conformation as a good agreement between sub-molecularly resolved STM images, and their frontier molecular orbitals in the gas phase are generally observed.⁵¹ The calculations were performed with the Gaussian 03 program package.⁵² The calculated frontier orbitals of the investigated oligopyridines are all of similar shape, with slight differences (Figure 14). The highest electron density is located at the pyrimidine ring and the benzene ring of the molecules, decaying to the terminal pyridines. Though the presented STM images do not reveal the exact shape of the calculated frontier orbitals, the overall shape of both the HOMO (highest occupied molecular orbital) and LUMO (lowest unoccupied molecular orbital) is expressed in the observed tunnel contrast of the molecules. The STM images of **4** (Figure 12) and **2** (Figure 7) exhibit clearly the overall molecular shape and therefore can be considered as mixture of the HOMO and the LUMO. The STM images of **1** (Figure 4) and **3** (Figures 9 and 10) from PO do not show the B-pyridine moieties, a fact that corresponds very well with the electron distribution of the HOMO. With the knowledge of the electron distribution on the frontier orbitals near the Fermi level, it is also possible to interpret nonsubmolecularly resolved STM images (Figure 8a). The highest electron density for both the HOMO and the LUMO is located on the pyrimidine ring. Hence, we assign the bright spots visible in the STM image of **3** in 1,3-DCB (Figure 8a) to the pyrimidine moieties of the oligopyridines.

Conclusion

Three new oligopyridines have been studied considering their self-assembly behavior at the HOPG/liquid interface and have been compared with an already known oligopyridine. They are

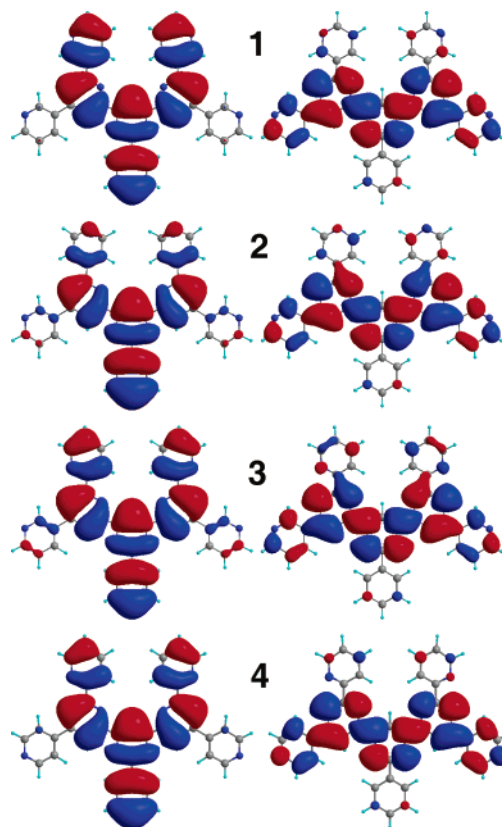


Figure 14. Hartree-Fock calculation (6-31G(d,p)-basis set) of the HOMO (left) and LUMO (right) in the coplanar conformation of oligopyridines **1–4**.

all constitutional isomers, exhibiting the same overall molecular shape. A systematic change in the position of the nitrogen atoms in the terminal pyridine units caused different monolayer patterns, investigated by STM. The 2D ordering behavior of the oligopyridines is mainly governed by subtle hydrogen-bonding interactions. It follows a simple concept based on geometric considerations leading to either linear or cyclic arrangements of the molecules. Additionally, it could be shown that, besides changes of the molecular constitution, the choice of the solvent plays an important role for the self-assembly, also, expressing different nanopatterns for the same molecules. Further investigations on the influence of the solvent on the 2D self-assembly are under work by varying systematically the solvents with and without H-bonding capabilities. Additional experiments on the formation of monolayers of the oligopyridines on different substrates under UHV conditions without the influence of any solvent are ongoing. The interaction energy of a pyridine dimer was calculated at the ab initio level, confirming the existence of $\text{C}-\text{H}\cdots\text{N}$ interactions between individual molecules. The observed monolayers exhibit functional subunits (coordination sites) and highly ordered voids which might be exploited as potential binding sites for several guests such as, for example, small molecules or metal ions and clusters. With these results, the weak $\text{C}-\text{H}\cdots\text{N}$ interaction between pyridine moieties emphasizes the pool of building blocks in crystal engineering and surface nanopatterning.

Experimental Section

General. The syntheses of the oligopyridines **3** and **4** and of bispyridinium salt **6** are already described.²⁸ The ketones **5a** and **b** were synthesized according to the literature.¹⁰ NH_4OAc and methanol were obtained from commercial sources and used

as received. The oligopyridines were purified before analytical measurements under vacuum and 200 °C for one week to remove volatile impurities. The NMR data were obtained on a Bruker DRX 500 at 500.1 MHz (¹H) and 125.8 MHz (¹³C), respectively. Chemical shifts are given in ppm relative to [D₂]TCE (¹H = 5.91 ppm, ¹³C = 74.2 ppm). The solvents for the STM measurements, TCB (1,2,4-trichlorobenzene) (+99%), 1,3-DCB (1,3-dichlorobenzene) (98%), and PO (1-phenyloctane) (99%), were used as received from Aldrich.

STM Investigations. The STM measurements were performed at the liquid/solid interface under ambient conditions with a low-current RHK 1000 STM system. All three compounds were dissolved in the appropriate solvents (see text) to give concentrated solutions. Generally, after examination of the quality of the mechanically edged Pt/Ir tip (90/10 or 80/20) through atomic resolution of the freshly cleaved surface of highly oriented pyrolytic graphite (HOPG, SPI-grade 3, SPI), a drop of the concentrated solution was applied to the surface with the tip in tunnel contact.⁵³ All STM images were recorded in constant current mode with a negative sample bias. The presented images are checked for reproducibility in several sessions using different tips and are derived from raw data without being subject to any manipulation or image processing except slope compensation. The distances and angles were determined by using an internal calibration.

Bis(terpyridine) 1. Bispyridinium salt **6** (1.20 g, 1.85 mmol), ketone **5a** (0.77 g, 3.70 mmol), and NH₄OAc (10.2 g, 132 mmol) in MeOH (30 mL) were heated under reflux overnight. After the mixture had been cooled to RT, the resulting solid was filtered, washed three times with MeOH, and dried in vacuo. Yield: 235 mg (13%). Mp: 369 °C. ¹H NMR ([D₂]TCE, 500.1 MHz, 100 °C): 9.66 (s, 1H; H₅), 9.45 (d, *J* = 1.7 Hz, 2H; H_{2''}), 9.09 (d, *J* = 1.7 Hz, 2H; H_{2'''}), 8.73 (m, 6H, H_{2''''}, 5', 6'''), 8.60 (td, *J* = 6.4, 1.7 Hz, 2H; H_{4''}), 8.11 (td, *J* = 8.2, 1.6 Hz, 2H; H_{4'''}), 8.07 (d, *J* = 1 Hz, 2H; H_{2''''}), 7.58–7.50 (m, 7H; H_{3''''}, 4''', 5'', 5'''). ¹³C NMR ([D₂]TCE, 100.6 MHz): 164.7, 164.3, 155.9, 155.7, 150.7, 150.6, 148.6, 148.1, 148.5, 138.0, 134.4, 134.1, 131.1, 128.8, 128.7, 124.0, 123.8, 119.7, 119.0, 118.9, 112.6. Anal. Calcd (%) for C₄₀H₂₆N₈ (618.70): C, 77.65; H, 4.24; N, 18.11. Found: C, 77.35; H, 4.41; N, 18.00.

Bis(terpyridine) 2. Bispyridinium salt **6** (1.20 g, 1.85 mmol), ketone **5b** (0.77 g, 3.70 mmol), and NH₄OAc (6.8 g, 88.2 mmol) in MeOH (30 mL) were heated under reflux overnight. After the mixture had been cooled to RT, the solid was filtered, washed three times with MeOH, and dried in vacuo. Yield: 0.79 g (69%). Mp: 344 °C. ¹H NMR ([D₂]TCE, 500.1 MHz, 100 °C): 9.68 (s, 1H; H₅), 9.09 (d, *J* = 2 Hz, 2H; H_{2''}), 8.95 (d, *J* = 1.5 Hz, 2H; H_{3'}), 8.81 (dd, *J* = 6, 1.6 Hz, 4H; H_{2'''}, 6'''), 8.75 (dd, *J* = 4.8, 1.6 Hz, 2H; H_{6''}), 8.69 (dd, *J* = 8, 1.7 Hz, 2H; H_{4''}), 8.15 (dd, *J* = 4.5, 1.6 Hz, 4H; H_{5'''}, 3'''), 8.11–8.08 (m, 4H; H_{5', 2''''}), 7.58–7.51 (m, 3H; H_{3''''}, 4'''), 7.48 (ddd, *J* = 7.9, 5, 0.6 Hz, 2H; H_{5''}). ¹³C NMR ([D₂]TCE, 125.3 MHz): 164.8, 164.1, 155.8, 155.4, 150.7, 148.5, 148.3, 145.8, 137.9, 134.5, 133.9, 131.1, 128.8, 128.7, 124.0, 121.2, 120.1, 119.8. Anal. Calcd (%) for C₄₀H₂₆N₈ (618.70): C, 77.65; H, 4.24; N, 18.11. Found: C, 77.38; H, 4.24; N, 17.74.

Acknowledgment. We thank the German Science Foundation (“Deutsche Forschungsgemeinschaft”) for financial support within the framework of the Research Center 569 (“Sonderforschungsbereich”) at the University of Ulm.

References and Notes

(1) Lehn, J.-M. *Supramolecular Chemistry: Concepts and Perspectives*; VCH: Weinheim, Germany, 1995.

- (2) Sauvage, J.-P.; Hosseini, M. W., Eds. *Templating, Self-Assembly and Self-Organization*; Pergamon: New York, 1996; Vol. 9.
- (3) Lei, S. B.; Yin, S. X.; Wang, H. N.; Xi, F.; Liu, H. W.; Wang, L. J.; Bai, C. L. *J. Phys. Chem. B* **2001**, *105*, 10838.
- (4) Lackinger, M.; Griessl, S.; Markert, T.; Jamitzky, F.; Heckl, W. M. *J. Phys. Chem. B* **2004**, *108*, 13652.
- (5) Lu, J.; Lei, S.-B.; Zeng, Q.-D.; Kang, S.-Z.; Wang, C.; Wan, L.-J.; Bai, C.-L. *J. Phys. Chem. B* **2004**, *108*, 5161.
- (6) De Feyter, S.; De Schryver, F. C. *J. Phys. Chem. B* **2005**, *109*, 4290.
- (7) Griessl, S.; Lackinger, M.; Edelwirth, M.; Hietschold, M.; Heckl, W. M. *Single Mol.* **2002**, *3*, 25.
- (8) Wintgens, D.; Yablon, D. G.; Flynn, G. W. *J. Phys. Chem. B* **2003**, *107*, 173.
- (9) De Feyter, S.; Gesquiere, A.; Abdel-Mottaleb, M. M.; Grim, P. C.; De Schryver, F. C. *Acc. Chem. Res.* **2000**, *33*, 520.
- (10) Clair, S.; Pons, S.; Seitsonen, A. P.; Brune, H.; Kern, K.; Barth, J. V. *J. Phys. Chem. B* **2004**, *108*, 14585.
- (11) Cai, Y.; Bernasek, S. L. *J. Am. Chem. Soc.* **2004**, *126*, 14234.
- (12) Plass, K. E.; Kim, K.; Matzger, A. J. *J. Am. Chem. Soc.* **2004**, *126*, 9042.
- (13) Dmitriev, A.; Spillmann, H.; Lingenfelder, M.; Lin, N.; Barth, J. V.; Kern, K. *Langmuir* **2004**, *20*, 4799.
- (14) Jonkheijm, P.; Miura, A.; Zdanowska, M.; Hoeben, F. J. M.; De Feyter, S.; Schenning, A. P. H. J.; De Schryver, F. C.; Meijer, E. W. *Angew. Chem.* **2004**, *116*, 76.
- (15) Gesquiere, A.; Jonkheijm, P.; Hoeben, F. J. M.; Schenning, A. P. H. J.; De Feyter, S.; De Schryver, F. C.; Meijer, E. W. *Nano Lett.* **2004**, *4*, 1175.
- (16) Freund, J. E.; Edelwirth, M.; Kröbel, P.; Heckl, W. M. *Phys. Rev. B* **1997**, *55*, 5394.
- (17) Gesquiere, A.; Abdel-Mottaleb, M. M. S.; De Feyter, S.; De Schryver, F. C. *Langmuir* **2000**, *16*, 10385.
- (18) De Feyter, S.; Larsson, M.; Schuurmans, N.; Verkuijl, B.; Zorinants, G.; Gesquiere, A.; Abdel-Mottaleb, M. M.; van Esch, J.; Feringa, B. L.; van Stam, J.; De Schryver, F. C. *Chem.-Eur. J.* **2003**, *9*, 1198.
- (19) Schuurmans, N.; Uji-i, H.; Mamdouh, W.; De Schryver, F. C.; Feringa, B. L.; van Esch, J.; De Feyter, S. *J. Am. Chem. Soc.* **2004**, *126*, 13884.
- (20) Swarbrick, J. C.; Ma, J.; Theobald, J. A.; Oxtoby, N. S.; O'Shea, J. N.; Champness, N. R.; Beton, P. H. *J. Phys. Chem. B* **2005**, *109*, 12167.
- (21) Keeling, D. L.; Oxtoby, N. S.; Wilson, C.; Humphry, M. J.; Champness, N. R.; Beton, P. H. *Nano Lett.* **2003**, *3*, 9.
- (22) Kim, K.; Plass, K. E.; Matzger, A. J. *Langmuir* **2005**, *21*, 647.
- (23) Mamdouh, W.; Uji-i, H.; Gesquiere, A.; De Feyter, S.; Amabilino, D. B.; Abdel-Mottaleb, M. M. S.; Veciana, J.; De Schryver, F. C. *Langmuir* **2004**, *20*, 9628.
- (24) Qian, P.; Nanjo, H.; Yokoyama, T.; Suzuki, T. M.; Akasakab, K.; Orhuib, H. *Chem. Commun.* **2000**, 2021.
- (25) Barth, J. V.; Weckesser, J.; Cai, C.; Günter, P.; Bürgi, L.; Jeandupeux, O.; Kern, K. *Angew. Chem.* **2000**, *112*, 1285.
- (26) Lingenfelder, M. A.; Spillmann, H.; Dmitriev, A.; Stepanow, S.; Lin, N.; Barth, J. V.; Kern, K. *Chem.-Eur. J.* **2004**, *10*, 1913.
- (27) Yokoyama, T.; Yokoyama, H.; Kamikado, T.; Okuno, Y.; Mashiko, S. *Nature* **2001**, *413*, 619.
- (28) Ziener, U.; Lehn, J.-M.; Mourran, A.; Möller, M. *Chem.-Eur. J.* **2002**, *8*, 951.
- (29) Stepanow, S.; Lin, N.; Vidal, F.; Landa, A.; Ruben, M.; Barth, J. V.; Kern, K. *Nano Lett.* **2005**, *5*, 901.
- (30) Vidal, F.; Delvigne, E.; Stepanow, S.; Lin, N.; Barth, J. V.; Kern, K. *J. Am. Chem. Soc.* **2005**, *127*, 10101.
- (31) Zell, P.; Mögele, F.; Ziener, U.; Rieger, B. *Chem. Commun.* **2005**, 1294.
- (32) Mourran, A.; Ziener, U.; Möller, M.; Breuning, E.; Ohkita, M.; Lehn, J.-M. *Eur. J. Inorg. Chem.* **2005**, 2641–2647.
- (33) Kröhnke, F. *Synthesis* **1976**, 1.
- (34) Durinda, J.; Szűcs, L.; Krasnec, L.; Heger, J.; Springer, V.; Kolena, J.; Keleti, J. *Acta Fac. Pharm. Bohemoslov.* **1966**, 89.
- (35) Yablon, D. G.; Guo, J. S.; Knapp, D.; Fang, H. B.; Flynn, G. W. *J. Phys. Chem. B* **2001**, *105*, 4313.
- (36) Fisher, A. J.; Blöchl, P. E. *Phys. Rev. Lett.* **1993**, *70*, 3263.
- (37) Böhringer, M.; Morgenstern, K.; Schneider, W.-D.; Berndt, R.; Mauri, F.; De Vita, A.; Car, R. *Phys. Rev. Lett.* **1999**, *83*, 324.
- (38) Sowerby, S. J.; Heckl, W. M.; Peterson, G. B. *J. Mol. Evol.* **1996**, *43*, 419.
- (39) Venkataraman, B.; Breen, J. J.; W. Flynn, G. *J. Phys. Chem.* **1995**, *99*, 6608.
- (40) Li, C.-J.; Zeng, Q.-D.; Wang, C.; Wan, L.-J.; Xu, S.-L.; Wang, C.-R.; Bai, C.-L. *J. Phys. Chem. B* **2003**, *107*, 747.
- (41) Nishino, T.; Bühlmann, P.; Itob, T.; Umezawa, Y. *Phys. Chem. Chem. Phys.* **2001**, *3*, 1867.
- (42) Mamdouh, W.; Uji-i, H.; Dulcey, A. E.; Percec, V.; De Feyter, S.; C., D. S. *Langmuir* **2004**, *20*, 7678.

- (43) Augusti, D. V.; Carazza, F.; Augusti, R.; Tao, W. A.; Cooks, R. G. *Anal. Chem.* **2002**, *74*, 3458.
- (44) Julian, R. R.; Hodyss, R.; Kinnear, B.; F. Jarrold, M.; Beauchamp, J. L. *J. Phys. Chem. B* **2002**, *106*, 1219.
- (45) Lackinger, M.; Griessl, S.; Heckl, W. M.; Hietschold, M.; Flynn, G. W. *Langmuir* **2005**, *21*, 4984.
- (46) Hanan, G. S.; Lehn, J.-M.; Kyritsakas, N.; Fischer, J. *Chem. Commun.* **1995**, 765.
- (47) Hanan, G. S.; Schubert, U. S.; Volkmer, D.; Riviere, E.; Lehn, J.-M.; Kyritsakas, N.; Fischer, J. *Can. J. Chem.* **1997**, *75*, 169.
- (48) Bassani, D. M.; Lehn, J.-M.; Baum, G.; Fenske, D. *Angew. Chem., Int. Ed. Engl.* **1997**, *36*, 1845.
- (49) Ohkita, M.; Lehn, J.-M.; Baum, G.; Fenske, D. *Chem.—Eur. J.* **1999**, *5*, 3471.
- (50) Coussan, S.; Brenner, V.; Perchard, J. P.; Zheng, W. Q. *J. Chem. Phys.* **2000**, *113*, 8059.
- (51) Strohmeier, R.; Petersen, J.; Gompf, B.; Eisenmenger, W. *Surf. Sci.* **1998**, *418*, 91.
- (52) Frisch, M. J.; Trucks, G. W.; Schlegel, H. B.; Scuseria, G. E.; Robb, M. A.; Cheeseman, J. R.; Montgomery, J. A., Jr.; Vreven, T.; Kudin, K. N.; Burant, J. C.; Millam, J. M.; Iyengar, S. S.; Tomasi, J.; Barone, V.; Mennucci, B.; Cossi, M.; Scalmani, G.; Rega, N.; Petersson, G. A.; Nakatsuji, H.; Hada, M.; Ehara, M.; Toyota, K.; Fukuda, R.; Hasegawa, J.; Ishida, M.; Nakajima, T.; Honda, Y.; Kitao, O.; Nakai, H.; Klene, M.; Li, X.; Knox, J. E.; Hratchian, H. P.; Cross, J. B.; Bakken, V.; Adamo, C.; Jaramillo, J.; Gomperts, R.; Stratmann, R. E.; Yazyev, O.; Austin, A. J.; Cammi, R.; Pomelli, C.; Ochterski, J. W.; Ayala, P. Y.; Morokuma, K.; Voth, G. A.; Salvador, P.; Dannenberg, J. J.; Zakrzewski, V. G.; Dapprich, S.; Daniels, A. D.; Strain, M. C.; Farkas, O.; Malick, D. K.; Rabuck, A. D.; Raghavachari, K.; Foresman, J. B.; Ortiz, J. V.; Cui, Q.; Baboul, A. G.; Clifford, S.; Cioslowski, J.; Stefanov, B. B.; Liu, G.; Liashenko, A.; Piskorz, P.; Komaromi, I.; Martin, R. L.; Fox, D. J.; Keith, T.; Al-Laham, M. A.; Peng, C. Y.; Nanayakkara, A.; Challacombe, M.; Gill, P. M. W.; Johnson, B.; Chen, W.; Wong, M. W.; Gonzalez, C.; Pople, J. A. *Gaussian 03*, revision B.04; Gaussian, Inc.: Wallingford, CT, 2004.
- (53) Rabe, J. P. *Ultramicroscopy* **1992**, *42*, 41.